Figure S1

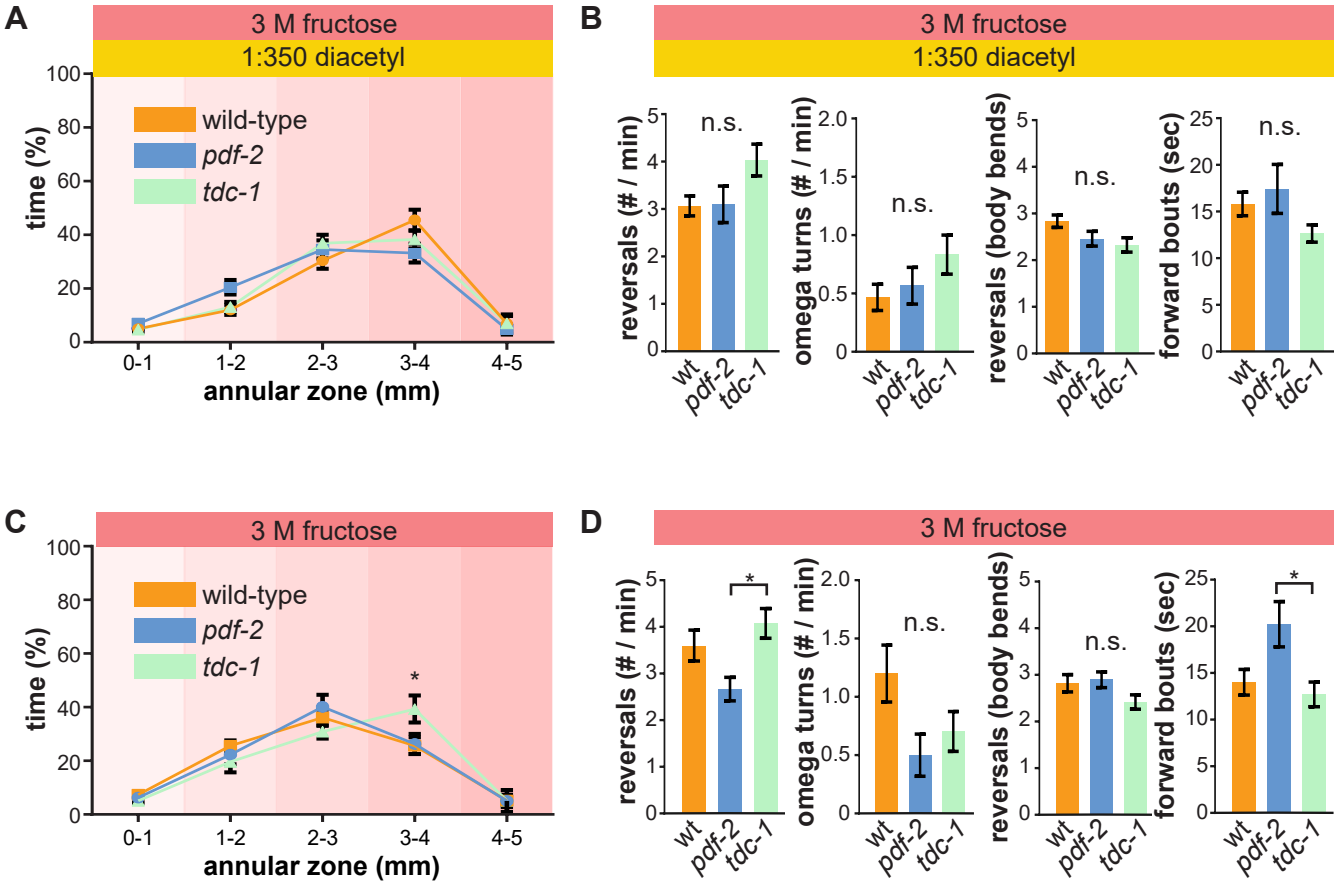
A
3 M fructose
1:350 diacetyl
wild-type
pdf-2
tdc-1
time (%)
annular zone (mm)
0-1
1-2
2-3
3-4
4-5
B
3 M fructose
1:350 diacetyl
reversals (# / min)
omega turns (# / min)
reversals (body bends)
forward bouts (sec)
n.s.
wt
pdf-2
tdc-1
C
3 M fructose
wild-type
pdf-2
tdc-1
time (%)
annular zone (mm)
*
D
3 M fructose
reversals (# / min)
omega turns (# / min)
reversals (body bends)
forward bouts (sec)
*
n.s.
wt
pdf-2
tdc-1

Figure S2

A

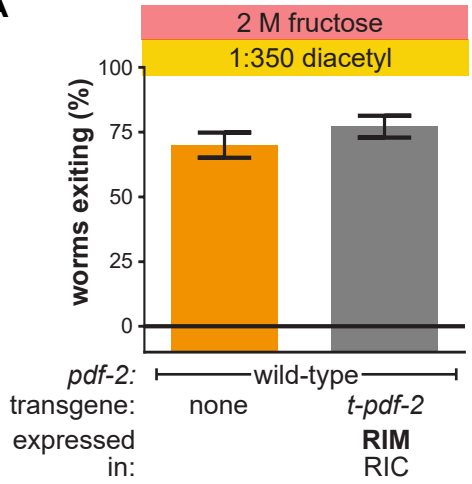
2 M fructose
1:350 diacetyl
worms exiting (%)
100
75
50
25
0
pdf-2:
wild-type
transgene:
none
t-pdf-2
expressed in:
RIM
RIC

Figure S3

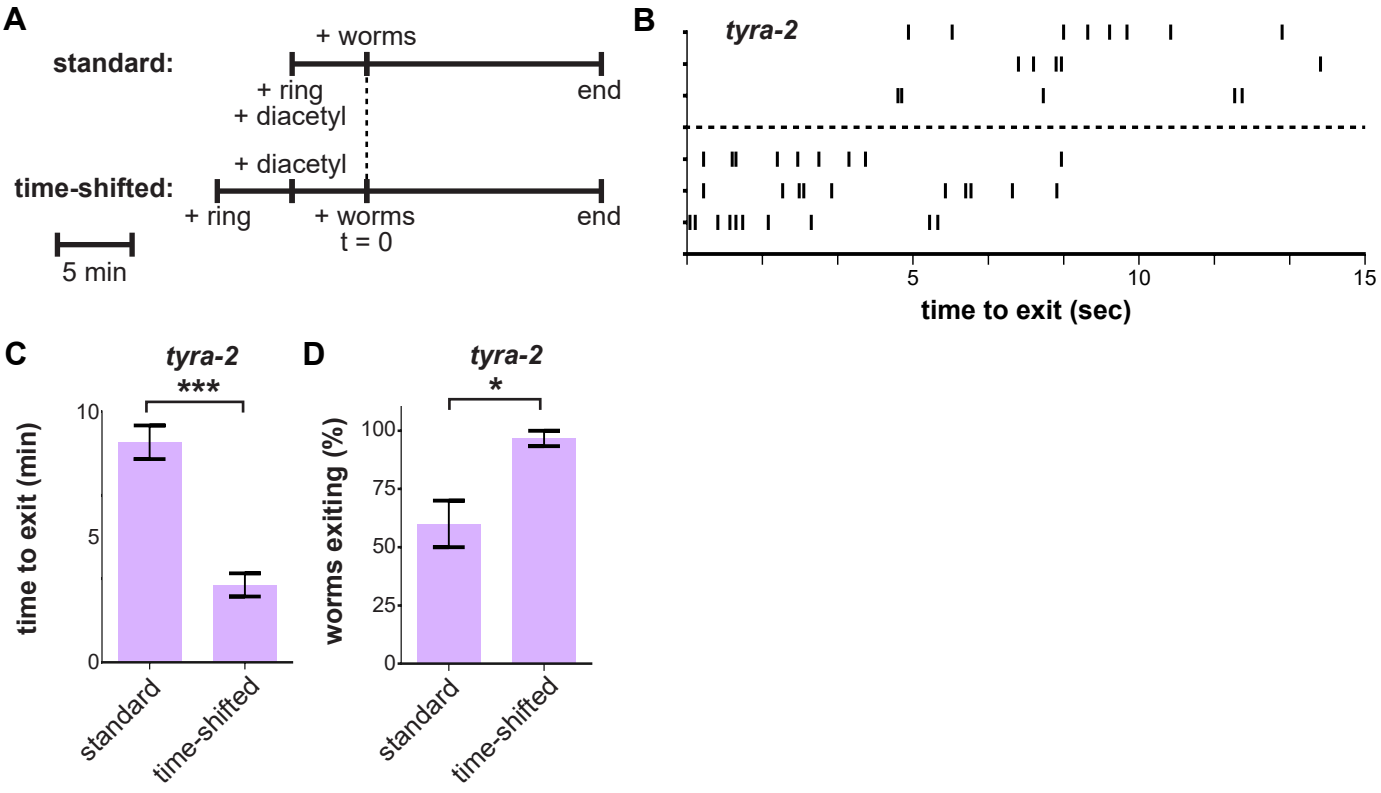
A
standard:
+ worms
+ ring
+ diacetyl
end
time-shifted:
+ diacetyl
+ ring
+ worms
t = 0
end
5 min
B
tyra-2
5
10
15
time to exit (sec)
C
tyra-2
***
time to exit (min)
10
5
0
standard
time-shifted
D
tyra-2
*
worms exiting (%)
100
75
50
25
0
standard
time-shifted

Figure S4

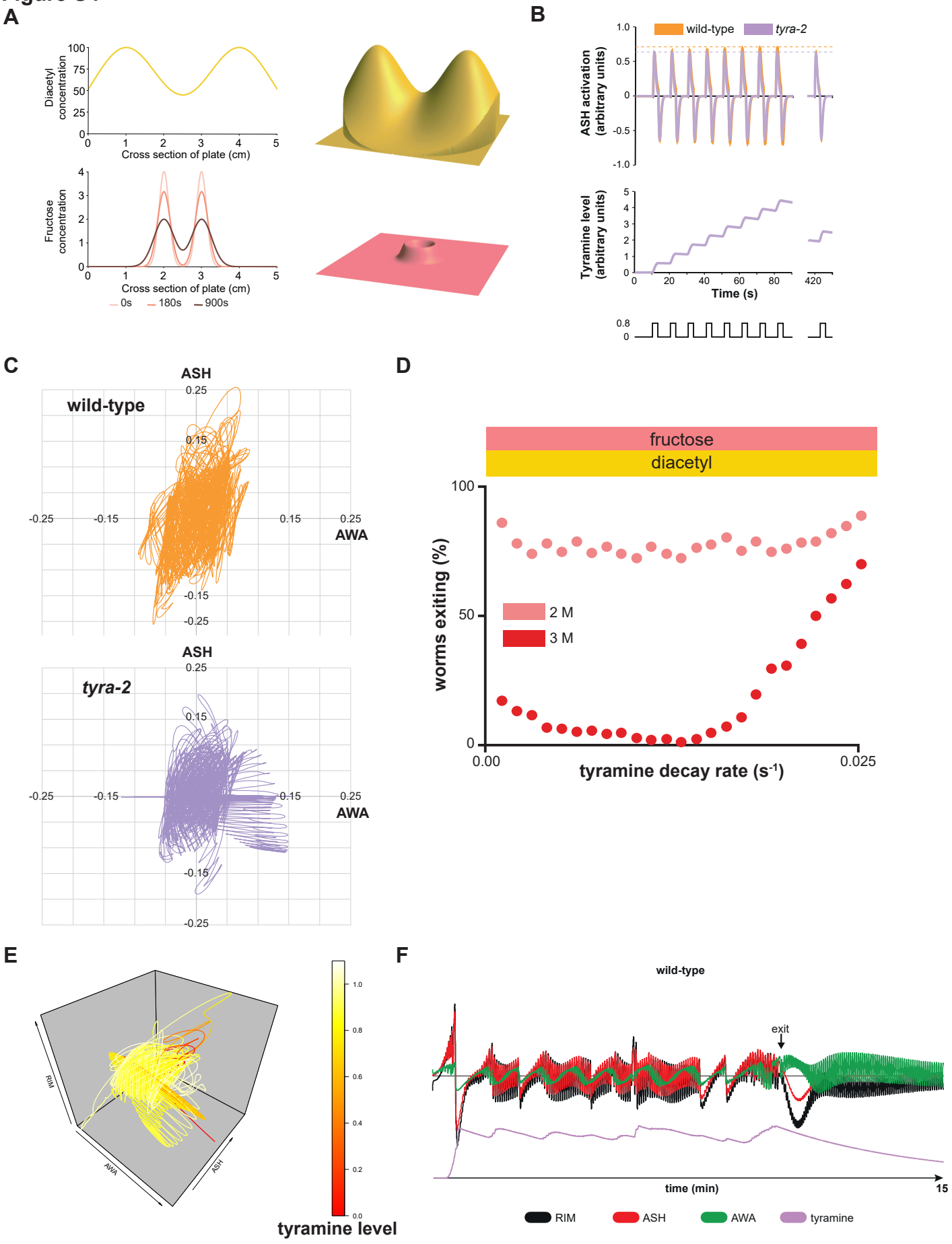
A
Diacetyl concentration
Cross section of plate (cm)
Fructose concentration
Cross section of plate (cm)
0s
180s
900s
B
wild-type
tyra-2
ASH activation (arbitrary units)
Tyramine level (arbitrary units)
Time (s)
C
ASH
wild-type
AWA
ASH
tyra-2
AWA
D
fructose
diacetyl
worms exiting (%)
2 M
3 M
tyramine decay rate (s-1)
E
RIM
AWA
ASH
tyramine level
F
wild-type
exit
time (min)
RIM
ASH
AWA
tyramine

Figure S5

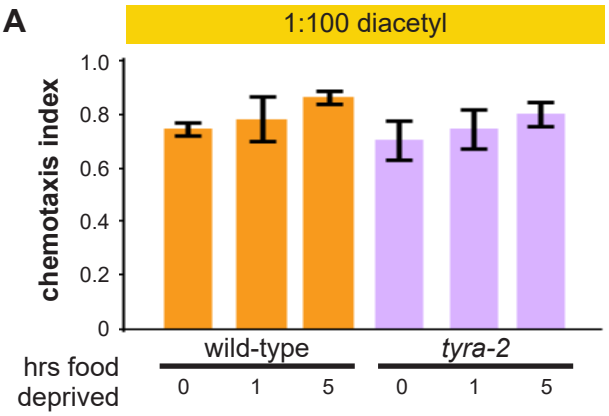
A
1:100 diacetyl
chemotaxis index
1.0
0.8
0.6
0.4
0.2
0
wild-type
tyra-2
hrs food deprived
0
1
5
0
1
5

Figure S6

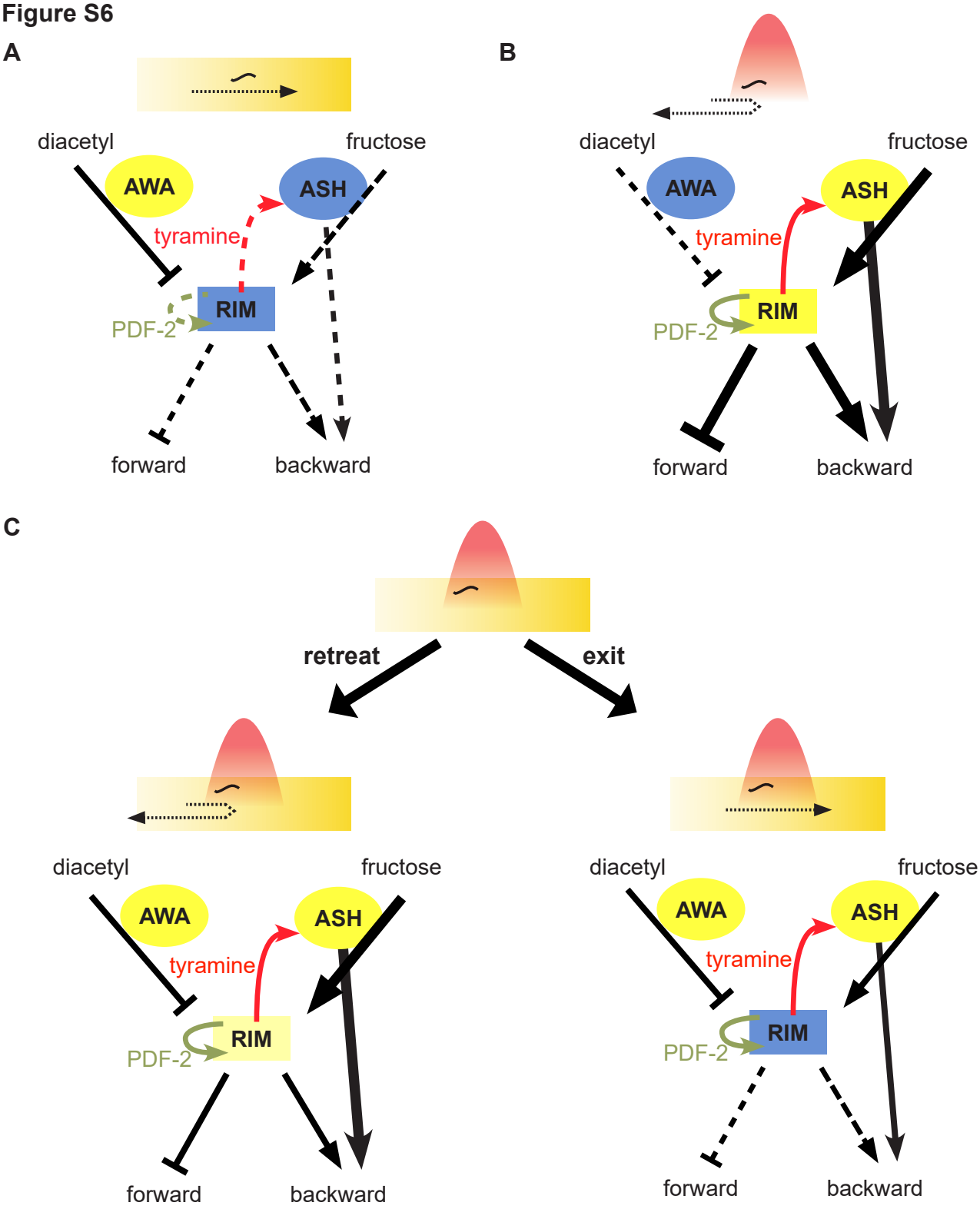
A
diacetyl
fructose
AWA
ASH
tyramine
RIM
PDF-2
forward
backward
B
diacetyl
fructose
AWA
ASH
tyramine
RIM
PDF-2
forward
backward
C
retreat
exit
diacetyl
fructose
AWA
ASH
tyramine
RIM
PDF-2
forward
backward
diacetyl
fructose
AWA
ASH
tyramine
RIM
PDF-2
forward
backward

Figure S1, related to Figures 2,3. Kinematic analysis of *pdf-2* and *tdc-1* null mutants

(A) Wild-type, *pdf-2*, and *tdc-1* null-mutant worms spend indistinguishable fractions of time in each of the radial zones of the osmotic ring in the presence of food odor. This excludes the potential confound that wild-type and mutant worms spend different amounts of time near the barrier, and thus have an altered opportunity to interact with it. (n=7-10 worms for each genotype, F = 1.273, p = 0.265)

(B) General defects in locomotion are not involved in aberrant multisensory decision making by *pdf-2* and *tdc-1* null-mutant worms. Kinematic parameters are indistinguishable between wild-type, *pdf-2* and *tdc-1* null-mutant worms as they navigate within the ring in the multisensory context.

(C) Wild-type and *pdf-2*, but not *tdc-1* null-mutant worms, spend indistinguishable fractions of time in each of the radial zones of the fructose ring in the absence of food odor (N=7-10 worms for each genotype, F = 2.510, p = 0.015). *tdc-1* null-mutant worms spend increased time in the 3-4 mm radial zone (*, p vs wild-type = 0.009).

(D) *pdf-2* and *tdc-1* null-mutant worm locomotor kinematics differ from one another as they navigate within the ring in the absence of food odor.

Figure S2, related to Figure 3. PDF-2-PDFR-1 autocrine loop is maximally active

(A) Expression of t-PDF-2 in RIM and RIC in a wild-type background did not suppress exiting of a 2 M fructose ring in the presence of diacetyl.

Figure S3, related to Figure 4. Diffusion of osmotic ring determines time to exit

(A) Schematic depicting protocols for determining effect of diffusion of osmotic ring on time to exit. Worms were either confronted with standard or time-shifted osmotic rings. Time-shifted rings are allowed five more minutes to diffuse than standard rings.

(B) Ethogram of time-to-exit reveals that *tyra-2* null-mutant worms exit time-shifted rings earlier than standard rings.

(C) Average time-to-exit of *tyra-2* null-mutant worms. Worms exit time-shifted rings approximately five minutes before standard rings.

(D) More worms exit time-shifted rings than standard rings in the 15 minute trial.

Figure S4, related to Figure 5. Time constants of accumulation and decay of tyramine signals determine multisensory decision balance

(A) Profiles of diacetyl and fructose concentration in simulated decision arena. While the bilobed diacetyl gradient is modeled as invariant over the time course of the decision, the simulated fructose gradient becomes shallower over time.

(B) Model ASH responses to repetitive fructose stimulation. In wild-type worms, the ASH response increases with every consecutive stimulus presentation due to increasing tyramine levels. This effect is not observed in *tyra-2* null-mutants. That tyramine potentiates ASH osmosensitivity by acting on TYRA-2 is somewhat surprising given that TYRA-2 has been characterized as a $G_{i/o}$-coupled receptor (Rex et al., 2005). However, invertebrate tyramine receptors have demonstrated the capacity to signal through $G_{i/o}$ while still increasing intracellular calcium (Rex et al., 2005; Rex and Komuniecki, 2002; Rex et al., 2004; Wragg et al., 2007).

(C) 2D phase space profile of ASH (y-axis) and AWA (x-axis) neuronal activity in a virtual wild-type worm (top) that remains inside the ring for the duration of the assay and a *tyra-2* null-mutant worm (bottom) that exits the ring. These phase space profiles demonstrate how the magnitude of ASH oscillatory activity is greater in wild-type

worms than in *tyra-2* null-mutant worms; in contrast, in *tyra-2* null-mutant worms, the AWA signals are larger, before dominating as the worm exits.

(D) Slow tyramine signals (decay constants of $0.001s^{-1}$ to $0.025s^{-1}$) in the model are necessary for wild-type worms to remain confined in the 3 M fructose ring, as observed experimentally. As tyramine decay becomes faster, wild-type worms begin exiting in substantial numbers. *n*=250 simulated worms per genotype and condition.

(E) 3D phase space profile of neuronal activity and tyramine level in a virtual wild-type worm that exits a 3 M fructose ring in the presence of diacetyl, with RIM inhibited to ~0.03 to simulate one-hour of food deprivation. This analysis (shown dynamically in **Supplemental Movie 1**) demonstrates several distinct phases in neuronal activity over the course of the decision. Progression through the phases depends on accumulation of tyramine signals that reinforce ASH activity upon repeated encounters with the ring. Initial oscillations are primarily in the ASH-RIM plane (red) as the animal nears and retreats from the fructose ring, leading to a slow accumulation of tyramine (white). The gradual diffusion of the fructose ring eventually results in the decay of tyramine levels and activity in RIM and ASH responses (yellow, then orange). Phase space oscillations get smaller, and tilt toward the AWA-RIM plane, indicating a desensitization of ASH and potentiation of AWA as the worm continues to approach the ring. Exiting of the ring follows a dip in tyramine levels after nine minutes (yellow-orange). AWA activity begins to dominate, despite the subsequent rapid increase in tyramine and strong RIM-ASH oscillations as the animal exits the ring (white). As the worm crosses the peak of the fructose ring, it encounters the steepest diacetyl gradient, as indicated by the significant increase in AWA activity. Once outside the ring, AWA then decreases again as the worm navigates towards the diacetyl spot. Once the animal reaches the diacetyl spot, both ASH and AWA activity levels decay and ASH activity is nearly abolished (red).

(F) Neural activity and tyramine signal profiles of AWA, ASH, and RIM in a virtual wild-type worm that exits a 3 M fructose ring in the presence of diacetyl, with RIM inhibited to ~0.03 to simulate one-hour of food deprivation, corresponding to phase space profile depicted in **(D)**.

Figure S5, related to Figure 6. Chemotaxis to 1:100 diacetyl after food deprivation

(A) Chemotaxis to 1:100 diacetyl is unaffected by food deprivation.

Figure S6, related to Figure 7. Model for sensorimotor network control of multisensory threat-reward decision making

(A) In the unisensory attraction-only context, AWA inhibits RIM and RIM neither inhibits forward command nor excites backward command interneurons. Thus, the worm proceeds forward up the diacetyl odor gradient. Yellow represents strong activity, while blue represents weak activity. Thickness of solid lines represents strength of signals, and dashed lines represent inactive signals. Other synaptic routes by which AWA and ASH indirectly communicate with forward and backward command locomotor interneurons are not shown.

(B) In the unisensory aversion-only context, ASH activates RIM, triggering tyraminergic RIM-ASH positive feedback and further potentiating ASH osmosensitivity. This combined strong ASH and RIM activation strongly inhibits forward command and strongly excites backward command interneurons. Thus, the worm reverses and retreats from the osmotic barrier. However, because of the absence of AWA-mediated inhibition of RIM in the unisensory aversion-only context, RIM-ASH feedback is not required for retreat from the osmotic barrier.

(C) In the multisensory context where RIM is both inhibited by AWA and activated by ASH, the worm makes a probabilistic choice between retreat and exit based on the instantaneous stochastic state of the network as it interacts with the osmotic barrier. An increase in RIM activity state leads to reversal behaviors that promote retreat from threats; however, these reversal behaviors are probabilistic because instantaneous activity state of RIM itself is stochastic (Gordus et al., 2015). When instantaneous network activity is strong, combined RIM and ASH activity inhibits forward command and activates backward command interneurons to trigger a reversal and retreat from the osmotic barrier. When instantaneous network activity is weak, combined RIM and ASH activity is insufficient to inhibit forward command and excite backward command interneurons, and the worm proceeds forward through the barrier to exit the ring. Autocrine PDF-2 signaling to RIM increases the gain of the RIM-ASH positive feedback

loop, and is suppressed by food deprivation to increase threat tolerance. Longer time-scale tyraminergic feedback increases the likelihood that instantaneous RIM and ASH network activity is strong. Disruptions that break the positive feedback loop increase threat tolerance in the multisensory context by allowing AWA-mediated inhibition of RIM to dominate and prevent reversals.

Supplemental Movie, related to Figures 5,6 (Online-only)

(A) Phase space profile of neuronal activity and tyramine levels in a virtual wild-type worm that exits a 3 M fructose ring in the presence of diacetyl, with RIM inhibited to ~0.03 to simulate one-hour of food deprivation. Left: 10 second sliding window of AWA, ASH, and RIM activity levels, plotted in phase space. Color represents tyramine level. Top right: Corresponding time traces of AWA and ASH. Bottom right: simulated worm trajectory over the course of the decision. Note that the concentration gradient of fructose changes over time.

Supplemental Experimental Procedures

Strains

C. elegans strains were maintained on Nematode Growth Medium (NGM) agar plates with *E. coli* OP50 as a food source. All strains were derived from the Bristol N2 wild-type strain. Each strain was backcrossed to the wild-type N2 at least 3 times. At least three independent lines for all transgenic strains were generated and tested, and presented results are aggregates of the independent lines. Strains used for each figure are detailed below:

Figure 1: N2, *odr-10 (ky225)*

Figure 2: N2, CX14484 *pdf-2(tm4393)*, MNN1 *pdf-2(tm4393)*; *lin-15(n765ts)*; *mnnEx1 [pdf-2p::pdf-2; lin-15^{+}]*

Figure 3: N2, CX14484 *pdf-2(tm4393)*, MNN2 *pdf-2(tm4393)*; *lin-15(n765ts)*; *mnnEx2 [tdc-1p::pdf-2; lin-15^{+}]*, MNN3 *pdf-2(tm4393)*; *lin-15(n765ts)*; *mnnEx3 [tdc-1p::t-pdf-2; lin-15^{+}]*, MNN4 *pdf-2(tm4393)*; *lin-15(n765ts)*; *mnnEx4 [nmr-2p::t-pdf-2; lin-15^{+}]*, MNN5 *pdf-2(tm4393)*; *lin-15(n765ts)*; *mnnEx5 [tbh-1p::t-pdf-2; lin-15^{+}]*, MNN6 *pdf-2(tm4393)*; *lin-15 (n765ts)*; *mnnEx6 [tdc-1p::t-scr; lin-15^{+}]*, MT13113 *tdc-1(n3419)*, MT9455 *tbh-1(n3247)*, MNN10 *pdf-2 (tm4393); tdc-1 (n3419)*

Figure 4: N2, MT13113 *tdc-1(n3419)*, QW245 *lgc-55(tm2913)*, VC125 *tyra-3(ok325)*, OH313 *ser-2 (pk1357)*, QW42 *tyra-2(tm1815)*, MNN7 *tyra-2(tm1815)*; *mnnEx7 [sra-6p::tyra-2; myo-3p::gfp]*, MNN8 *tyra-2(tm1815)*; *mnnEx8 [gpa-13p::tyra-2; myo-3p::gfp]*; MNN9 *tyra-2(tm1815)*; *mnnEx9 [mec-17p::tyra-2; myo-3p::gfp]*, XP631 *lite-1(ce314); kyEx2865 [sra-6p::GCaMP3, unc-122p::gfp]*; XP649 *lite-1(ce314); tyra-2(tm1846)*; *kyEx2865 [sra-6p::GCaMP3, unc-122p::GFP]*, MNN11 *pdf-2 (tm4393); tyra-2(tm1815)*

Figure 6: N2, QW42 *tyra-2(tm1815)*

Figure 7: N2, MT13113 *tdc-1(n3419)*, QW42 *tyra-2(tm1815)*, CX16632 *kyIs693 [pNP502(tdc-1::HisCl1::sl2::mcherry)]*

Supplemental Figure 1: N2, CX14484 *pdf-2(tm4393)*, MT13113 *tdc-1(n3419)*

Supplemental Figure 2: N2, MNN12 N2; *mnnEx9 [tdc-1p::t-pdf-2; myo-3p::gfp]*

Supplemental Figure 3: N2, QW42 *tyra-2(tm1815)*

Supplemental Figure 5: N2, QW42 *tyra-2(tm1815)*

Tethered peptides were designed as described previously (Choi et al., 2012; Choi et al., 2009; Choi and Nitabach, 2013; Fortin et al., 2009). Briefly, tethered peptides are chimeric fusion proteins with an N-terminal secretory signal sequence, followed by the sequence of the peptide of interest, a linker, and a C-terminal glycolipid anchor targeting signal. Tethered peptide transgenes were synthesized by Entelechon. Transgenes were synthesized with optimal *C. elegans* codon usage and optimal upstream Kozak sequences.

Amino acid sequences for construction of tethered peptides are as follows (peptide is **bold**, * indicates stop codon):

t-PDF-2:

MSALLILALVGAAVA**NNAEVVNHILKNFGALDRLGDV**GNEQKLISEEDLGNGAGFATPVTLALVPALLA
TFWSLL*

t-SCR:

MSALLILALVGAAVA**VIALDNKRNLNFENGAVGVHLD**GNEQKLISEEDLGNGAGFATPVTLALVPALLA
TFWSLL*

Transgenic strains were constructed by injection of plasmid DNA into the germline according to standard practice. Plasmid DNA was engineered using Multisite Gateway Cloning technology (Invitrogen, http://www.lifetechnologies.com/us/en/home.html). *pdf-2*, *t-pdf-2*, *t-scr*, and *tyra-2* protein coding sequences were cloned into pDONR-221 vectors. These were linked with cell-specific promoters *pdf-2*, *tdc-1*, *nmr-2*, *tbh-1*, *sra-6*, *gpa-13*, and *mec-17*. Promoters were generated by amplifying genomic DNA using Promoterome sequences (http://worfdb.dfci.harvard.edu/promoteromedb/) or published primer sequences and cloning them into pDONR-P4-P1R vectors. These were then integrated into final vectors, and injected at concentrations of 20-50 ng/µL. A *lin-15* rescue construct pL15EK or *myo-3::GFP* construct was co-injected to mark transformation.

Behavioral assays

For unisensory and multisensory assays, the fructose ring was constructed essentially as described (Culotti and Russell, 1978). Briefly, 10µL of fructose solution is applied in a 1cm diameter ring centered on a standard NGM plate. For multisensory assays, 1µL diluted diacetyl (1:350 in water) was applied to each side of the plate, at least 1cm from the ring border. Four minutes after construction of the ring, ten (unless otherwise indicated) 18-24 hours post-L4 stage adult worms were removed from a food plate, placed on a plate without food to remove attached bacteria, and then quickly transferred inside the ring. Fifteen minutes later, the number of worms outside the ring were counted. For the food deprivation assays, worms were transferred to a plate without food to remove attached bacteria, then quickly transferred to another plate without food for the indicated time interval. 10 mM or 30 mM histamine and 30 mM tyramine plates were prepared exactly as described previously (Jin et al., 2016; Pokala et al., 2014).

Chemotaxis assays were performed essentially as described, with minor changes from (Sengupta et al., 1996), as described below. First, a standard sized (5 cm) NGM plate was used. Second, similar to the multisensory assay, ten staged adult worms were placed at a location equidistant to the two spots, control and test, applied to either side of the plate. To remain consistent with the multisensory assay, chemotaxis was measured after 15 minutes. One-way ANOVA with Tukey-Kramer *post-hoc* test was used for statistical comparison with wild-type worms.

For kinematic analysis, assays prepared as detailed above were recorded using a Point Grey Grasshopper camera (GRAS-50S5C-C) filming at 7.5 fps. Dishes were illuminated with a red LED ring obtained from Moritex Schott (Model RLA-75X46-00R). These videos were then analyzed using commercially available WormLab software from MBF Bioscience (http://www.mbfbioscience.com/wormlab). Software provided *x-y* position information. A picture of the ring, taken immediately after the assay, was used to determine the center of the ring. Distance from the center of the ring was then calculated and sorted into annular zones. Two-way ANOVA with a *post-hoc* Tukey-Kramer test was used to determine statistically significant differences from wild-type. Other locomotor parameters were manually scored as previously described (Alkema et al., 2005; Donnelly et al., 2013; Gray et al., 2005; Pirri et al., 2009).

Imaging

Calcium imaging of ASH neurons was performed on young adult *lite-1 (ce314)* worms immobilized in an olfactory chamber as described previously (Chronis et al., 2007). Imaged worms expressed the genetically-encoded calcium sensor GCaMP3 from the *sra-6* promoter (Tian et al., 2009). Prior to loading into the olfactory chamber worms were bathed in neuronal buffer (10mM HEPES pH 7.1, 40mM NaCl, 1mM $MgSO_4$, 1mM tetramisole) for 10 min either in the presence or absence of 50mM tyramine. Once in the chamber worms were exposed to a laminar flow of neuronal buffer (with or without tyramine) for at least 10 sec before switching flow in the chamber to direct the test stimulus across the animal's nose (diluted in neuronal buffer containing 1mg/ml bromophenol blue). Bromophenol blue was added to monitor test stimulus flow and had no effect on ASH activity. Worms were exposed to the test stimulus for 20 sec. All imaging experiments were performed using a Nikon FN1 microscope equipped with a 40x water immersion objective. Images were captured at ~10Hz using a Photometrics CoolSnap EZ camera with a single frame exposure time of 100ms. Averaged fluorescence was calculated for a region of interest (ROI) surrounding the ASH soma and was background corrected using NIS Elements AR software. The percent change in fluorescence for each frame was calculated relative to the corrected fluorescence of the ROI just prior to stimulus onset.

Computational model

Model animals possess a simplified nervous system comprising sensory neurons AWA and ASH, interneuron RIM, and two reciprocally inhibited motor neurons denoted DMN and VMN, which activate dorsal and ventral body bends, respectively. Neurons are modeled as "leaky integrators," such that each neuron integrates its input over time, while subject to continuous decay ("leak") of activity. AWA and ASH sensory neurons respond with transient activation to changes in diacetyl or fructose stimuli, respectively. These transients were modeled with a fast depolarizing signal, which drives a delayed rectifying counter-signal. This sensory response was adapted from chemotaxis models in unicellular eukaryotes, in which the delayed signal modeled intracellular diffusion (Cohen and Sanders, 2014; Levine and Rappel, 2013). Neuronal time scales were set in accordance with calcium imaging data (Kato et al., 2014), and were fast enough to mediate steering responses on time scales of an undulation. Activation of model sensory neurons AWA and ASH instantaneously provides differentially weighted inhibitory and excitatory inputs onto RIM, respectively. RIM integrates these sensory inputs and inhibits motorneurons DMN and VMN to bias dorsal versus ventral bends, thereby inducing gradual steering of the worm. Additionally, RIM activity positively increases the likelihood of pirouettes, which are modeled as instantaneous step changes in angular heading. In the absence of sensory input, the model worm's dorsoventral undulatory locomotion is driven by stable oscillations of a simplified central pattern generating circuit consisting of DMN and VMN. The animals move forward along an undulating path at a fixed speed of 0.11mm/s, interrupted by occasional stochastic turning events (average pirouette rate of 2.1 turns/min). Sensory input allows both steering (klinotaxis), by biasing the oscillator, and a "tumble-and-run" strategy (klinokinesis), by varying the pirouette probability. Importantly, in addition to the above previously established feedforward sensorimotor pathways, the simulation includes RIM-ASH tyraminergic positive feedback. Tyraminergic potentiation of ASH in the model is only engaged above a threshold level of RIM activation (see **Equation M3**). This non-linear relationship ensures that the RIM-ASH positive feedback loop is activated only in response to sufficiently aversive stimuli, a feature of the model that is necessary to successfully reproduce experimental exiting rates. The TYRA-2 receptor in ASH promotes ASH sensitivity to osmotic stimuli in the presence of tyramine, but with no direct effect on the ASH membrane potential. *tyra-2* null-mutant worms are modeled as lacking this tyraminergic feedback to ASH. Food deprivation was modeled as direct inhibition of RIM activity.

Model parameters were manually calibrated until exiting rates of simulated wild-type and *tyra-2* null-mutant worms matched experimental exiting rates in multisensory and unisensory contexts for 2 M, 3 M, and 4 M fructose (compare **Figure 2B** with **Figure 5B**). Specifically, model parameters subject to calibration comprise: the strengths of the AWA-RIM and ASH-RIM synapses, the tyramine accumulation rate, the tyramine decay rate, and the threshold activity value above which tyramine is secreted from RIM. Of these, the first two were constrained by the experimental exiting rates of *tyra-2* null-mutant worms in the multisensory and unisensory contexts; the latter three were then calibrated to match the experimental exiting rates of wild-type worms in those same contexts.

The virtual decision arena comprises a continuously diffusing fructose gradient ring and time-invariant diacetyl gradients originating from two spots outside the ring (**Figure S4A**). Modeling the fructose gradient as dynamically changing was essential, as continued diffusion of the fructose ring influences the time and probability of exit in our experiments (**Figure S3**), and static fructose gradients failed to reproduce experimental exiting rates in the model. Each simulation begins with a single worm in the center of the virtual arena with a randomly selected initial heading, and the simulation is allowed to proceed for fifteen virtual minutes.

See accompanying **Supplemental Experimental Procedures** section for more details.

Supplemental References

Cohen, N., and Sanders, T. (2014). Nematode locomotion: dissecting the neuronal-environmental loop. Curr Opin Neurobiol *25*, 99-106.

Kato, S., Xu, Y., Cho, C.E., Abbott, L.F., and Bargmann, C.I. (2014). Temporal responses of C. elegans chemosensory neurons are preserved in behavioral dynamics. Neuron *81*, 616-628.

Levine, H., and Rappel, W.J. (2013). The physics of eukaryotic chemotaxis. Phys Today *66*.

Supplemental Experimental Procedures

Computational model

A computational simulation framework was developed to study *in silico* the behavior of single model worms confronted with the decision making assay. Our model of the animal assumes that during locomotion, the body follows the head, allowing us to focus on sensory-motor control of a point worm. Thus, at each point in time, animals are represented by their point coordinates $\vec{r}(t) = (x(t), y(t))$ and heading $\theta(t)$. Animals move at fixed speed and sense their environment using a simplified nervous system which dynamically controls their direction of locomotion.

Our computational model extends a previously developed *C. elegans* sensorimotor model that was extensively tested against a number of assays (Sanders T., PhD thesis 2016). To study sensory integration, our new model circuit contained two sensory neurons (AWA and ASH) and one interneuron (RIM) as well as a simplified motor system (Fig. M1). The motor output consists of undulations that are modulated by the sensory system to generate steering, and instant turning events representing pirouettes. All neuronal equations and parameters, including the sensory responses, interneuron and motor neuron dynamics were taken without modification from our previous model, in which they were constrained by calcium imaging data (Thiele et al., 2009; Larsch et al., 2013) and published behavioral data (Iino and Yoshida, 2009; Jansen et al., 2002; Hukema et al., 2006, 2008).

To extend the model to cope with sensory integration, we began by modeling the assay environment and specifically the fructose and diacetyl concentration profiles over time (Fig. M3). The addition of RIM to our model circuit required synaptic connections from ASH and from AWA onto RIM. The two synaptic weights were set by matching behavioral data from *tyra-2* animals (Fig. 5). Next, RIM's tyramine accumulation threshold and the tyramine accumulation and decay rates were set, based on behavioral results from wild type animals (Fig. 5). Thus, only five of the model parameters were free. One additional variable (the RIM rest potential) was needed to capture food deprivation results; the corresponding results are presented as a parameter sweep. This incremental modeling approach ensures the model is maximally constrained and is aimed at enhancing its predictive potential.

1.1 Model neurons

As the AWA, ASH and RIM Left/Right neuronal pairs are all coupled by gap junctions (White et al., 1986) and ASH Left and Right neurons are known to respond identically (Thiele et al., 2009), all three neuron pairs have been collapsed into single model neurons. We model all neurons as leaky integrators (with arbitrary units)

$$\tau_m \frac{dV_i}{dt} = -V_i + V_{0,i} + \sigma\left(I\right), \tag{M1}$$

where V_i is a voltage like variable for neuron i, also referred to here as neuronal activity; τ_m is a neuronal time constant; finally, $V_{0,i}$ represents the resting potential (set at 0). $\sigma(I)$ is a modified sigmoid function over the input

$$\sigma\left(I\right) = \tanh\left(bI\right), \tag{M2}$$

where b is a gain parameter. Thus a neuron's activation ranges from -1 to 1 and converges to $V_{0,i} + \sigma(I)$ with a timescale of τ_m. This formulation is borrowed from rate neuron models

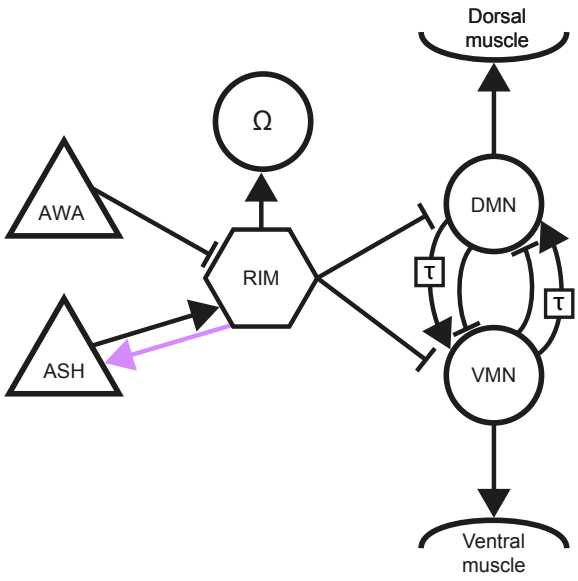

Figure M1: *The model sensorimotor system consists of two sensory neurons, AWA and ASH (triangles), a single interneuron, RIM (hexagon), and a motor circuit (circles). RIM integrates over inputs from the sensory neurons and projects to all three units of the motor circuit. The extrasynaptic neuropeptide tyramine mediates the feedback signal from RIM to ASH. A half-center oscillator (DMN, VMN) acts as a central pattern generator for ongoing undulations that is subject to a steering bias from the sensory inputs. The delay τ is modeled as an implicit neuron. The muscles are included in the diagram for ease of visualization only. An abstract turn component Ω drives pirouettes.*

and naturally leads to thresholding and saturation of activation, as observed in *C. elegans* sensory neurons (Suzuki et al., 2008; Thiele et al., 2009; Larsch et al., 2013).

The input term I sums over all synaptic and sensory contributions $I = I_{\text{syn}}(t) + I_{\text{sens}}(t)$, where $I_{\text{syn}} = \sum_j w_{ij} V_j$ is a weighted sum over all presynaptic neuron activations. The sensory contributions I_{sens} are given in Equations (M5)–(M7). Note that since synapses are not rectified, hyperpolarizing a neuron will effectively reverse the sign of its synaptic outputs (with hyperpolarizing and depolarizing postsynaptic transmission across excitatory and inhibitory synapses respectively). Food deprivation is modeled as sustained inhibition of RIM, by suppressing the RIM resting potential, $V_{0,\text{RIM}}$. The tyramine signal, denoted here $T(t)$, is modeled according to

$$\frac{dT}{dt} = \alpha_{\text{tyr}} H(V - V_{\text{tyr}}) - \beta_{\text{tyr}} T \,, \tag{M3}$$

where the function $H(x) = x$ for $x > 0$ and 0 otherwise. In other words, the tyramine level $T \geq 0$ at all times and increases only when RIM activity is above an activity threshold V_{tyr}.

Neuron parameters	Value	Description
τ_m	0.5 s	Neuronal time constant
$V_{0,i}$	0	Resting potential
b	2	Activation gain factor (used in sigmoid function)
α_{tyr}	$0.4\,\text{s}^{-1}$	Tyramine integration rate
β_{tyr}	$0.004\,\text{s}^{-1}$	Tyramine decay rate
V_{tyr}	0.05	Tyramine accumulation threshold
Synaptic weights	**Value**	**Description**
$w_{\text{AWA,RIM}}$	-0.4	AWA onto RIM
$w_{\text{ASH,RIM}}$	0.75	ASH onto RIM
$w_{\text{RIM,XMN}}$	-0.5	RIM onto DMN and VMN
$w_{\text{RIM},\Omega}$	1	RIM onto Ω
$w^{+}_{\text{D,V}}$	0.88	DMN to VMN excitation (to, from hidden neuron)
$w^{+}_{\text{V,D}}$	0.88	VMN to DMN excitation (to, from hidden neuron)
$w^{-}_{\text{D,V}}$	-1.4	DMN to VMN inhibition
$w^{-}_{\text{V,D}}$	-1.4	VMN to DMN inhibition

1.1.1 RIM inhibition

As mentioned above, food deprivation was mimicked in our model using a single pathway: sustained RIM inhibition, implemented as a modulated RIM resting potential $V_{0,\text{RIM}} \leq 0$. To parametrize the food deprivation effect on RIM, we fit the exit rate as function of the RIM inhibition by the logit link function. A maximum likelihood best fit was found using the glm function in the R statistical language (R Core Team, 2014). The resulting fit is the inverse-logit (logistic) function:

$$P[y(x)] = \frac{1}{1+\exp[-y(x)]} = \frac{1}{1+\exp(-\beta_0-\beta_1 x)}\,, \tag{M4}$$

where x is the RIM inhibition and $y(x)$ is the exit rate. The parameters for the four fits, which we dub RIM inhibition coefficients, are given in the table below.

RIM inhibition coefficient	Value	Description
β_0	-3.022	Intercept, diacetyl and fructose, wild type
β_1	117.006	Coefficient, diacetyl and fructose, wild type
β_0	-0.988	Intercept, diacetyl and fructose, *tyra*-2 null
β_1	87.403	Coefficient, diacetyl and fructose, *tyra*-2 null
β_0	-6.393	Intercept, fructose, wild type
β_1	135.158	Coefficient, fructose, wild type
β_0	-3.830	Intercept, fructose, *tyra*-2 null
β_1	99.109	Coefficient, fructose, *tyra*-2 null

Experimental food deprivation data points were matched visually to RIM inhibition values by matching the percentage of wild type animals exiting the ring in the fructose only assay. If multiple RIM inhibition strengths provided an equal fit, virtual *tyra*-2 null mutant data points were used in addition to pick the best matching RIM inhibition value.

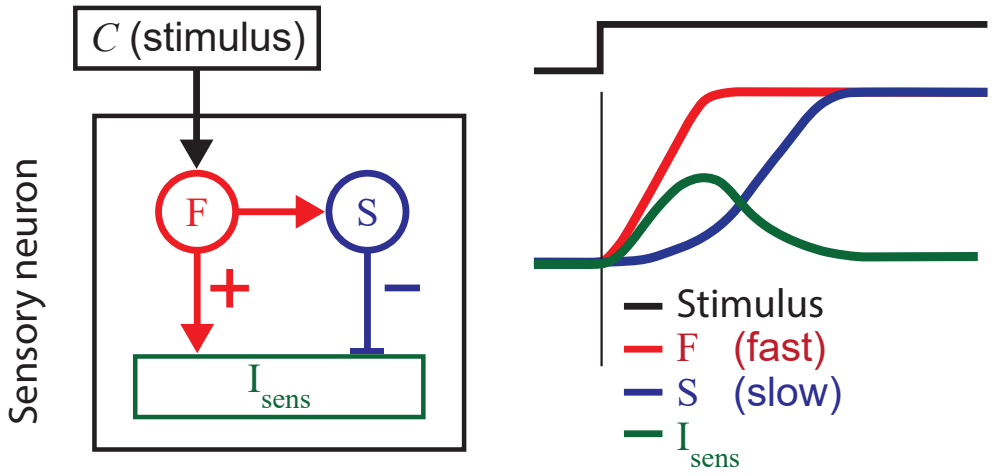

Figure M2: ***Left****: Model sensory neurons exhibit a transient response to changes in concentrations. The response is mediated by a fast component (F) that drives a slow delayed-rectifier component (S).* ***Right****: Schematic traces of the response to a concentration step change, showing the fast (F) and slow (S) components and the overall transient response (I_{sens}).*

For the assay with diacetyl and fructose, the estimates from the fructose only assay were used.

Sensory Neurons

Calcium imaging data has shown that the responses of many sensory neurons in *C. elegans* roughly approximate a low-pass filtered time derivative over their respective inputs (Hilliard et al.; Suzuki et al., 2008; Thiele et al., 2009; Kato et al., 2014; Larsch et al., 2013). In many cases, changes in stimuli selectively produce a response with a characteristic rise time, followed by a slower decay to a baseline (i.e., rest). In particular, AWA and ASH respond with a transient depolarization to stimulus upsteps, and with a transient hyperpolarization to stimulus downsteps (Thiele et al., 2009; Larsch et al., 2013). The biphasic nature of the derivative-like responses seen in AWA and ASH suggests sensory neurons use two components with opposite effect and a separation of timescales (Kato et al., 2014). Accordingly, in our model the sensory neuron response I_{sens} is given by the difference between a fast component F and a slow (delayed-rectifying) component S (Figure M2)

$$I_{\text{sens}} = F - S\,. \tag{M5}$$

The fast component F integrates over the sensory stimulus $C = C(x, y, t)$ (here the concentration of the respective signal) with a characteristic rate α_i and decays at rate β_i. The slow component S follows F with a delay, producing the characteristic biphasic response

Sensory neuron parameters	Value	Description
α_{AWA}	$4\,s^{-1}$	AWA depolarization rate
β_{AWA}	$15\,s^{-1}$	AWA depolarization leak rate
γ_{AWA}	$2\,s^{-1}$	AWA rectification (repolarization) rate
$\bar{\alpha}_{\text{ASH}}$	$4\,s^{-1}$	ASH depolarization rate
β_{ASH}	$15\,s^{-1}$	ASH depolarization leak rate
γ_{ASH}	$2\,s^{-1}$	ASH rectification (repolarization) rate

(Figure M2):

$$\frac{dF}{dt} = \alpha_i\, C - \beta_i F\,, \tag{M6}$$

$$\frac{dS}{dt} = \gamma_i (F - S)\,. \tag{M7}$$

The physiological mechanism by which TYRA-2 modulates ASH excitability is unknown. The application of tyramine did not appear to affect the ASH membrane potential. Instead, when a hyperosmotic stimulus was applied in the presence of tyramine, the ASH response appeared enhanced compared to the response in the absence of tyramine (main text Fig. 4). Consistent with these observations, here the effect of TYRA-2 on ASH excitability is modeled as a contribution to the neuronal activation rate $\bar{\alpha}_{\text{ASH}}$

$$\alpha_{\text{ASH}}(t) = \bar{\alpha}_{\text{ASH}} + T(t). \tag{M8}$$

Initially, the activity of the neurons, all neuron components and the tyramine level are set to 0.

Motor system

Model animals move at a constant speed while the direction of motion is modulated by two separate motor programs: a stochastic pirouette command unit and a central pattern generating undulation circuit consisting of two motor neurons, denoted VMN and DMN (Figure M1). Reciprocal inhibition between VMN and DMN supports a half-center oscillator that generates and maintains stable oscillations (representing the animal's undulatory locomotion). This reciprocal connectivity pattern is reminiscent of connectivity found in several classes of head motor neurons in *C. elegans*.

The oscillator subcircuit includes delayed excitatory connections (Figure M1). To simplify our model, we used 'hidden' interneurons to create a delayed connection from VMN to DMN and vice versa. Thus, the delayed excitatory connection from VMN to DMN is implemented as two connections, one from VMN to the hidden interneuron, and another from the hidden interneuron to DMN, using the neuronal time constant of the hidden interneuron (τ_m) as a synaptic delay.

In the absence of a sensory input, this subcircuit will produce stable oscillations, facilitated by fast reciprocal inhibition and delayed reciprocal excitation (Figure M1). Any activity in one of the oscillating neurons will cause fast inhibition, followed by slower excitation of the other which in turn leads to recurrent inhibition. Thus the frequency and amplitude of the oscillations are determined by the timescales of the neurons (τ_m), the

connection strengths of the reciprocal inhibition, and delay in the reciprocal excitatory connections. When both neurons are equally active, the circuit does not oscillate. However, any small difference in activity is amplified by the mutual inhibition. Thus neuronal fluctuations would ensure stable oscillations even in a symmetric circuit. For simplicity, in the model, simulations are initiated with brief, equal and opposite input pulses into the two motor neurons VMN and DMN. Input from RIM into VMN and DMN biases the undulations to mediate steering.

Similar to other computational models of *C. elegans* (Bryden and Cohen, 2004, 2008; Izquierdo and Lockery, 2010), the direction of locomotion (θ) evolves as a function of the difference of the dorsal and ventral activation:

$$\frac{d\theta}{dt} = \omega \left(V_{\mathrm{VMN}} - V_{\mathrm{DMN}} \right), \tag{M9}$$

where ω sets the undulation amplitude. Point worms move with constant velocity $v = 0.11$ mm/s along a direction vector θ according to

$$\frac{d(x,y)}{dt} = (v \, \sin\theta, v \, \cos\theta) \, . \tag{M10}$$

Pirouettes are executed by resetting the orientation of movement of the point worm θ, to a random value between 0 and 2π drawn from a uniform distribution. The probability rate of a pirouette is given by the activation of the pirouette command unit (Ω) and given by a piece-wise linear monotonic function:

$$P_\Omega(V_\Omega) = \begin{cases} \overline{V}_\Omega + \epsilon & \overline{V}_\Omega + \epsilon \leq \overline{V}_\Omega + w_\Omega \; V_\Omega \\ \overline{V}_\Omega + w_\Omega \, V_\Omega & \overline{V}_\Omega - \epsilon \leq \overline{V}_\Omega + w_\Omega \; V_\Omega < \overline{V}_\Omega + \epsilon \\ \overline{V}_\Omega - \epsilon & \overline{V}_\Omega + w_\Omega \; V_\Omega < \overline{V}_\Omega - \epsilon \end{cases} \tag{M11}$$

where V_Ω denotes the activity of the abstract pirouette neuron, $\overline{V}_\Omega$ is the mean pirouette rate (over the domain), and the proportionality constant is set to $w_\Omega = 2.1$.

Motor output	**Value**	**Description**
v	$0.11\,\mathrm{mm}\,s^{-1}$	Forward speed
V_{start}	0.001	Oscillator start signal
τ_{start}	0.01 s	Duration of oscillator start signal
w_Ω	2.1	$P_\Omega(V_\Omega)$ proportionality constant
$\overline{V}_\Omega$	$0.035\,s^{-1}$	Mean pirouette rate
ϵ	$0.035\,s^{-1}$	Pirouette rate variation amplitude

All assays are simulated on a virtual two dimensional 5 cm plate, which animals cannot leave. All coordinates are given relative to an origin at the center of the arena.

1.2 Decision making assay

A virtual decision making assay was implemented to reproduce our experimental assay. The fructose ring, $\mathrm{FR}(\vec{r}, t)$ was modeled by continuous diffusion from an initial condition of a 1 cm diameter, placed in the center of the arena. Due to the radial symmetry of the

Assay parameter	Value	Description
τ_{end}	900 s	Duration of the assay
δt	0.0001 s	Integration time step of the simulation
$\vec{r}(0) = (x(0), y(0))$	(0, 0) cm	Initial worm positions
$\theta(0)$	U(0, 2π)	initial direction drawn from uniform distribution
V_i	0	Initial activity for all neurons
F_i	0	Initial value: fast component, all sensory neurons
S_i	0	Initial value: slow component, all sensory neurons
$T(0)$	0	Initial value of Tyramine
t_{FR}	300 s	Fructose diffusion time prior to assay start
$\vec{r}_{\text{FR}} = (x_{\text{FR}}, y_{\text{FR}})$	(0, 0) cm	Center of fructose ring
R	0.5 cm	Fructose ring radius
D_{FR}	3×10^{-5} cm^2/s	Fructose ring diffusion coefficient
C_{FR}	20, 30, 40	Fructose coefficients for 2, 3 and 4 M respectively
t_{DA}	60 s	Diacetyl diffusion time prior to assay start
$\vec{r}^{\,1,2}_{\text{DA}} = (x^{1,2}_{\text{DA}}, y^{1,2}_{\text{DA}})$	$(\pm 1.5, 0)$ cm	Center of diacetyl spots
D_{DA}	2.52×10^{-4} cm^2/s	Diacetyl diffusion coefficient
C_{DA}	100	Diacetyl amplitude

problem, assuming an initial narrow ring at R and neglecting the boundary conditions at the edge of the plate, the exact solution to the fructose diffusion in two dimensions is given by

$$\mathrm{C}(\vec{r}, t) = M_0 \int_0^\infty d\lambda \; \lambda \, e^{-\lambda^2 D_{\text{FR}}\, t} J_0(\lambda R)\, J_0(\lambda r)\,, \tag{M12}$$

where $r = |\vec{r}|$, J_0 is the zeroth regular Bessel function and M_0 is a normalization constant. Sufficiently close to the ring, the solution is well approximated by a one dimensional diffusion along the polar coordinate r:

$$\mathrm{FR}(r, t) = C_{\text{FR}} \left(\frac{t_{\text{FR}}}{t_{\text{FR}} + t}\right)^{\frac{1}{2}} \left(\exp\left[-\frac{(r-R)^2}{4D_{\text{FR}}(t_{\text{FR}} + t)}\right] + \exp\left[-\frac{(r+R)^2}{4D_{\text{FR}}(t_{\text{FR}} + t)}\right]\right). \tag{M13}$$

Here t_{FR} denotes the time of fructose diffusion prior to the start of the experiment at $t = 0$, when virtual worms are added to the simulation. The coefficient C_{FR} incorporates the concentration, diffusion coefficient factor and sensory neuron receptor strengths, and is referred to for simplicity as a concentration. The two exponentials correspond to contributions from the two edges of the ring: The closer edge at a distance $r - R$ from the worm and the farther edge at a distance $r + R$. The concentration and diffusion coefficient were set to match experimental results with different durations of fructose diffusion t_{FR}.

Visual inspection of experimental worm traces showed animals moving towards diacetyl peaks even after 15 minutes. This is consistent with continuing evaporation of diacetyl, leading to an sustained concentration gradient throughout the assay. To capture this, we approximated the diacetyl concentration profile $\mathrm{DA}(x, y, t)$, by a two phased process: an initial rapid diffusion (to establish the concentration profile from two initial spots), followed by a static field:

$$\mathrm{DA}(x, y, t) = C_{\text{DA}} \sum_{i=1}^{2} \exp\left(-\frac{(x - x^i_{\text{DA}})^2 + (y - y^i_{\text{DA}})^2}{4D_{\text{DA}}\, t_{\text{DA}}}\right), \tag{M14}$$

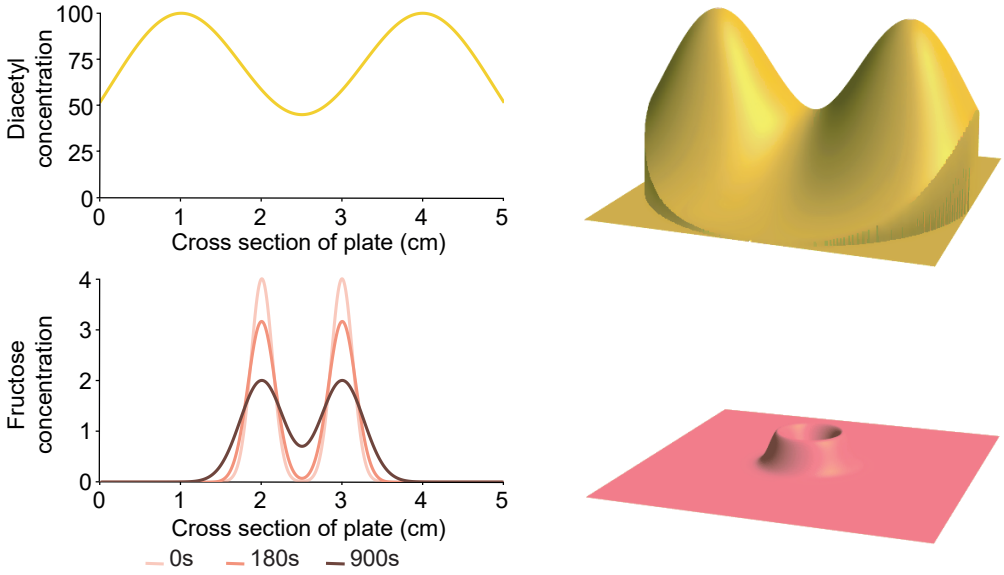

Figure M3: *Concentration profiles (cross sections and corresponding top-down views) used in the* in silico *decision making assay.* ***Top:*** *Steady state diacetyl profile resulting from two diacetyl sources at* ± 1.5 *cm from the center.* ***Bottom:*** *Snapshots of fructose concentration profile due to diffusion from a 1 cm diameter ring.*

where $(x^i_{\mathrm{DA}}, y^i_{\mathrm{DA}})$ are the coordinates for the i^{th} diacetyl spot and t_{DA} denotes the duration of diacetyl diffusion.

At $t = 0$ a single worm is placed at the center of the arena. Numerical integration of its nervous system and motor control is implemented with Euler integration, with a fixed integration time step (0.1 ms). As in the experimental assay, the balance of attraction and repulsion was quantified by the percentage of independently simulated worms that have exited the ring by 900 seconds.

References

J. Bryden and N. Cohen. Neural control of *Caenorhabditis elegans* forward locomotion: the role of sensory feedback. *Biological Cybernetics*, 98(4):339–351, 2008. doi: 10.1007/s00422-008-0212-6.

J. A. Bryden and N. Cohen. A simulation model of the locomotion controllers for the nematode *Caenorhabditis elegans*. In S. Schaal, A. Ijspeert, A. Billard, S. Vijayakumar, J. Hallam, and J.-A. Meyer, editors, *From Animals to Animats 8: Proceedings of the Eighth International Conference on the Simulation of Adaptive Behavior*, pages 183–192, July 2004.

M. A. Hilliard, A. J. Apicella, R. Kerr, H. Suzuki, P. Bazzicalupo, and W. R. Schafer. *In vivo* imaging of *C. elegans* ash neurons: cellular response and adaptation to chemical repellents. *EMBO Journal*, 24.

R. K. Hukema, S. Rademakers, M. P. J. Dekkers, J. Burghoorn, and G. Jansen. Antagonistic sensory cues generate gustatory plasticity in *Caenorhabditis elegans*. *EMBO Journal*, 25:312–322, 2006.

R. K. Hukema, S. Rademakers, and G. Jansen. Gustatory plasticity in *C. elegans* involves integration of negative cues and nacl taste mediated by serotonin, dopamine, and glutamate. *Learning and Memory*, 15:829–836, 2008.

Y. Iino and K. Yoshida. Parallel use of two behavioral mechanisms for chemotaxis in *Caenorhabditis elegans*. *The Journal of Neuroscience*, 29:5370–5380, 2009.

E. J. Izquierdo and S. R. Lockery. Evolution and analysis of minimal neural circuits for klinotaxis in *Caenorhabditis elegans*. *The Journal of Neuroscience*, 30:12908–12917, 2010.

G. Jansen, D. Weinkove, and R. H. A. Plasterk. The g-protein gamma subunit gpc-1 of the nematode *C. elegans* is involved in taste adaptation. *EMBO Journal*, 21:986–994, 2002. doi: 10.1093/emboj/21.5.986.

S. Kato, Y. Xu, C. E. Cho, L. F. Abbott, and C. I. Bargmann. Temporal responses of *C. elegans* chemosensory neurons are preserved in behavioral dynamics. *Neuron*, 81(3): 616–628, 2014.

J. Larsch, D. Ventimiglia, C. I. Bargmann, and D. R. Albrecht. High-throughput imaging of neuronal activity in *Caenorhabditis elegans*. *Proceedings of the National Academy of Sciences of the United States of America*, 110(45):E4266–E4273, 2013. doi: 10.1073/pnas.1318325110.

R Core Team. *R: A Language and Environment for Statistical Computing*. R Foundation for Statistical Computing, Vienna, Austria, 2014. URL `http://www.R-project.org/`.

H. Suzuki, T. R. Thiele, S. Faumont, M. Ezcurra, S. R. Lockery, and W. R. Schafer. Functional asymmetry in *Caenorhabditis elegans* taste neurons and its computational role in chemotaxis. *Nature*, 454(7200):114–117, 2008. doi: 10.1038/nature06927.

T. R. Thiele, S. Faumont, and S. R. Lockery. The neural network for chemotaxis to tastants in *Caenorhabditis elegans* is specialized for temporal differentiation. *The Journal of Neuroscience*, 29(38):11904–11911, 2009.

J. G. White, E. Southgate, J. N. Thomson, and S. Brenner. The structure of the nervous system of the nematode *C. elegans*. *Philosophical Transactions of the Royal Society London B Biological Sciences*, 314(1165):1–340, 1986.